A pragmatic approach for a 3D material model considering elasto-plastic behaviour, damage initiation by Puck or Cuntze and progressive failure of fibre-reinforced plastics

O. Völkerink[a,*], E. Petersen[a,b], J. Koord[a], C. Hühne[a]

[a]German Aerospace Center (DLR), Institute for Composite Structures and Adaptive Systems, Braunschweig, Germany
[b]Fraunhofer, Institute for Wind Energy Systems (IWES), Am Seedeich 45, 27572 Bremerhaven, Germany

Abstract

Fibre reinforced plastics with tough epoxy and thermoplastic matrices are spreading increasingly in many lightweight applications. For an efficient and reliable design the mechanical behaviour, considering non-linear plasticity, various failure modes under complex loading and damage progression, has to be estimated with numerical simulations. Most state-of-the-art continuum damage models do not consider the non-linear behaviour of the matrix material or are not suited for 3D solid elements. This work proposes a combined 3D continuum damage / plasticity model. It uses a single parameter flow criterion in combination with Cuntze's Failure Mode Concept (FMC) for intralaminar failure. The FMC requires no iterative fracture angle search as the Action Plane Strength Criterion by Puck (APSC). This work describes details of the developed model like the coupling of the FMC with a degradation model as well as the implementation into Abaqus / Standard. A validation against open-hole tension tests made out of AS4/PEEK from literature is performed. It can be shown that the prediction of experimental failure loads with the FMC as well as with the APSC provides comparable results. The maximum deviations are between -7.85%

---

*Corresponding author
Email address: `oliver.voelkerink@dlr.de` (O. Völkerink)

Preprint submitted to Computers & Structures *April 24, 2020*

and +12.85%. However, the computation times for predictions with the FMC are significantly less than with the APSC.

Keywords: Damage mechanics, Finite element analysis (FEA), Failure criterion, Non-linear behaviour, Plastic deformation, Fibre reinforced plastics

1. Introduction

The numerical prediction of strength and fracture behaviour is one of the most important factors for progress in the design of structures made of laminated fibre reinforced plastics (FRP). Due to the ability to tailor the mechanical properties such as stiffness and strength as well as a good fatigue resistance, these laminated composite materials are for instance widespread in the civil engineering, automotive, aerospace and ship building industry. Reliable numerical failure analyses are needed in the design of composite structures to support or even replace experimental tests. In this way, the cost- and time-intensive testing effort can be significantly reduced and the development process additionally accelerated.

Analysis approaches used in this context often assume laminate failure at first ply failure. This leads to a very conservative design since fibre composite structures can carry further loads after initial damage [1]. In order to achieve an efficient and reliable design of structures the mechanical behaviour up to total failure has to be estimated in the design phase with numerical simulations. This includes the consideration of damage initiation by various failure modes under complex loading as well as damage progression.

Most of the constitutive models consider composites on the mesoscale, i.e. ply by ply. Like the material model described in this work, these models are based on Continuum Damage Mechanics (CDM). The models are usually divided into three parts: A model for the mechanical behaviour prior to damage initiation, a failure criterion to be able to detect damage initiation and a description of the mechanical behaviour in the postfailure regime [2]. Many CDM-based models for composites have been developed in the past [3]. In order to give a brief overview a few selected models are discussed below.

Simple progressive damage models combine a linear-elastic constitutive formulation with a set of failure criteria for the different intralaminar failure types and a constant stiffness degradation, also called sudden degradation, after failure initiation [4, 5, 6]. A representative of this model class, in this case with the failure criterion of Hashin [7], is used by Hühne et al. [8] to perform progressive damage analyses of composite bolted joints. However, the majority of models use gradual degradation models [9, 10, 11]. These degradation models describe the decrease in stiffness due to damage as a linear or exponential function, which depends on the corresponding critical energy release rate. The main difference between the investigated models is the set of failure criteria used to detect failure initiation and whether they are formulated for the plane stress state or for the three-dimensional case. In the models mentioned above for example the failure criteria of Puck [12], the Tsai-Wu [13] or the LaRC03-04 criterion [14] are used. All of the previously mentioned models assume linear-elastic mechanical behaviour prior to damage initiation.

In contrast, several experimental findings reported in literature [15, 16, 17, 18], show a non-linearity prior to discrete damage such as fibre and interfibre failure or delaminations. This non-linearity originates from plasticity of the matrix material, fibre rotation and microcracks, what is often described as pseudo-plasticity. For example Wang and Callus [15] observed a hyperbolic in-plane shear stress-strain relation in AS4/3501-6 $[\pm 45°]_{4s}$ specimens tested under tensile loading. Van Paepegem et al. [16] tested specimens, made from Roviglas R17/475 glass fibre and Araldite LY 556 epoxy with a $[\pm 45°]_{2s}$ layup, in a cyclic tensile loading process and found permanent deformations after unloading. Similar irreversible strains were observed by Lafarie-Frenot and Touchard [17] when they tested $[\pm 45°]_{2s}$-specimens made from two different materials. One material was a thermoplastic fibre composite made from AS4/PEEK and the other material was a thermoset fibre composite made from T300/914. In addition, Vogler and Kyriakides [18] describe a non-linear stress-strain relationship in AS4/PEEK composite specimens loaded in shear, transverse compression and in an interaction of both loading cases.

These experimental findings show that the assumptions of a linear-elastic behaviour prior to damage is not valid for many FRP composite materials. For this reason, a material model is required that also takes this non-linearity prior to damage initiation into account. Lüders et al. [19] developed a model for fatigue lifetime predictions using the three-dimensional failure criterion by Puck which considers pre-failure non-linearities of the matrix. The non-linear relation between the shear stress τ and the shear strain γ is defined by an exponential function. A similar approach to describe the non-linear behaviour in shear is used by Donadon et al. [20], but instead of an exponential a polynomial cubic stress-strain relationship was applied. However, both models only consider a non-linearity prior to damage initiation for the shear components. A model with a different approach for the modelling of plasticity is described by Ernst et al. [21]. In their multiscale approach the plasticity is modelled on the micromechanical scale, where the behaviour of fibre and matrix is described with different material models. For the matrix an isotropic plastic flow potential depending on the first two stress invariants is used. The non-linear stress-strain relationships are then applied in meso- and macromechanical analyses. Vogler et al. [22] use a non-associated flow rule to account for the pre-failure non-linearities. However, six yield surface parameters and three plastic potential parameters are necessary for the model to describe the material behaviour.

In contrast, a transversally isotropic plasticity model with an associative flow rule was introduced by Sun and Chen [23]. The composite material is assumed to be linear-elastic in fibre direction. Only one coefficient is needed to describe the anisotropy in the plasticity. In total only three parameters are necessary. Due to its simplicity, this model was used by Chen et al. [2] and Din et al. [24] in combination with Hashin's and Puck's failure criterion respectively. Both models showed good results in the validation, but assume a plane-stress state and can therefore only be used with shell elements. Some authors report that the consideration of the general three-dimensional stress state increases the prediction accuracy [10, 25]. To add, as shown in [26], the failure criterion of Hashin does not describe the matrix damage with high accuracy. This is underlined by the second World-Wide Failure Exercise (WWFE-II), which showed that the failure criteria of Puck and Cuntze are able to describe those failure modes with higher accuracy [27] than the theory of Hashin. For this reason Din et al. [24] use Puck in combination with the one parameter plasticity model of Sun and Chen. However, the FMC of Cuntze [28] has the advantage over Puck [12] that no computational expensive iterative fracture angle search is needed for interfibre failure.

The provision of a material model, unlike [2] and [24], for the general three-dimensional case with the plasticity model of Sun and Chen in combination with Cuntze's less computational-intensive failure criterion is the motivation for the present work.

2. The 3D anisotropic damage / plasticity coupled constitutive model

The proposed material model can be divided into four components: Linear-elastic behaviour (1), plastic behaviour (2), damage initiation (3) and damage progression (4). These components are illustrated in the stress-strain plot in Fig. 1.

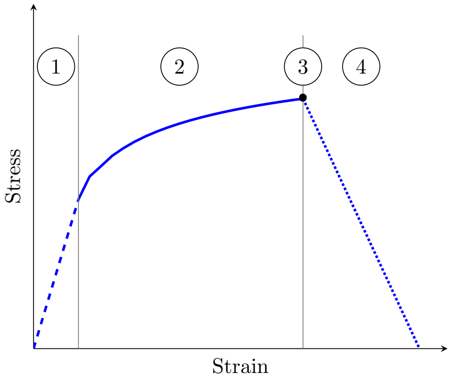

Figure 1: Stress-strain curve showing individual components of the proposed material model

The following section, which briefly describes the theories behind the individual components, is structured on the basis of this division.

2.1. Effective stress and damage operator

The material model developed in this work will be used to analyse macroscopic structures. For this reason, no discrete damage is modelled in the individual ply of the composite, but the approach of smeared damage according to Kachanov [29] is used. Under the assumption that the damage in the area under consideration is isotropic, it is assumed that the area available for the transfer of loads A_{eff} decreases in comparison with the undamaged area A_0. With this consideration an effective stress $\tilde{\sigma} = P/A_{eff}$ can now be defined to substitute the nominal stress $\sigma = P/A_0$. When damage has occured, the effective stress $\tilde{\sigma}$ is higher than the nominal stress σ at constant load P.

In accordance with the smeared damage of Kachanov [29], Matzenmiller et al. [30] describe a damage model for an orthotropic single ply, which is used in this work. A damage operator $\boldsymbol{M}(d)$ is defined, which establishes the relationship between the effective and the nominal stress:

$$\tilde{\sigma} = \boldsymbol{M}(d) \cdot \sigma \tag{2.1}$$

The damage operator or lamina damage tensor used in this work is constructed as follows:

$$\boldsymbol{M}(d) = diag\left[\frac{1}{1-d_f}; \frac{1}{1-d_m}; \frac{1}{1-d_m}; \frac{1}{1-d_s}; \frac{1}{1-d_s}; \frac{1}{1-d_m}\right] \tag{2.2}$$

In this case d_f is the damage variable associated with fibre failure. The damage variables d_m and d_s are associated with matrix failure under transverse respectively shear loading. These scalar damage variables take values between 0 and 1, where 0 represents the undamaged and 1 the completely damaged state. In the implementation the values for d are limited to 0.99 in order to avoid division by zero. In addition, the damage variables d_f and d_m distinguish between damage from tensile and compressive stresses. The following relationships are used to determine a smeared damage variable from the two loading types:

$$d_f = d_{ft} + d_{fc} - d_{ft} \cdot d_{fc} \tag{2.3}$$

$$d_m = d_{mt} + d_{mc} - d_{mt} \cdot d_{mc} \tag{2.4}$$

A detailed derivation of equations 2.3 and 2.4 can be found in [10]. Due to the plasticity in the composite material the total strain tensor ε results in the sum of the elastic strain tensor ε^e and the plastic strain tensor ε^p:

$$\varepsilon = \varepsilon^e + \varepsilon^p \tag{2.5}$$

The stress-strain relationship for the effective and the nominal stress tensor can be described according to the CDM theory and are suitable for a displacement-based Finite Element (FE) approach as follows:

$$\tilde{\sigma} = \boldsymbol{C}_0 \cdot \varepsilon^e; \qquad \sigma = \boldsymbol{M}(d)^{-1} \cdot \boldsymbol{C}_0 \cdot \varepsilon^e \tag{2.6}$$

2.2. Plasticity model

Like mentioned above, the plastic strain ε^p represents all irreversible deformations. The portion of plastic strain in the total strain and the stress corrected for plasticity are determined using a transversally isotropic plasticity model with an associative flow rule. Sun and Chen describe a plastic potential for anisotropic fibre composite materials [23]. Under the assumption of transverse isotropy in the 2-3 plane and linear-elastic behaviour in fibre direction $d\varepsilon_{11}^p = 0$, the plastic potential f for the three-dimensional case results to [31]:

$$f(\sigma_{ij}) = \frac{1}{2}\left[(\sigma_{22} - \sigma_{33})^2 + 4\tau_{23}^2 + 2a(\tau_{13}^2 + \tau_{12}^2)\right] \tag{2.7}$$

The parameter a in Eq. 2.7 weights the in-plane shear behaviour. This plastic potential was established based on the observation of Sun and Chen [23] on micromechanical models that only hydrostatic stresses cause plastic deformation. Eq. 2.8 describes the comparison between the yield limit $\bar{\sigma}_y(\tilde{p})$ and the effective stress $\bar{\sigma} = \sqrt{3f}$ in order to distinguish between the elastic and the plastic domain:

$$f(\tilde{\sigma}, \tilde{p}) = \sqrt{3f} - \bar{\sigma}_y(\tilde{p}) \leq 0 \tag{2.8}$$

The plastic potential can also be expressed in matrix/vector notation using the mapping matrix $\boldsymbol{P}$, cf. [32], which is used in the user defined material model (UMAT) implementation in this publication:

$$F(\tilde{\sigma}, \tilde{p}) = \frac{1}{2}\tilde{\sigma}^T : \boldsymbol{P} : \tilde{\sigma} - \bar{\sigma}_y^2(\tilde{p}) \tag{2.9}$$

For the plastic potential in Eq. 2.7, the mapping matrix $\boldsymbol{P}$ reads:

$$\boldsymbol{P} = \begin{bmatrix} 0 & 0 & 0 & 0 & 0 & 0 \\ & 3 & -3 & 0 & 0 & 0 \\ & & 3 & 0 & 0 & 0 \\ & & & 6a & 0 & 0 \\ & sym. & & & 6a & 0 \\ & & & & & 12 \end{bmatrix} \tag{2.10}$$

Taking into account the associated flow rule, the incremental plastic strain components can be expressed in terms of the plastic potential f where $d\lambda$ is the plastic multiplier:

$$d\varepsilon_{ij}^p = \frac{\partial f}{\partial \sigma_{ij}} d\lambda \tag{2.11}$$

From eq. 2.11 it can be seen that plastic strains are considered in all components except the fibre direction. As stated by Weeks and Sun [31], experiments have shown that FRP materials with a non-linear behaviour prior to damage, like thermoplastic fibre composites, do not have a defined yield point. Therefore, the yield limit $\bar{\sigma}_y(\tilde{p})$ is a function of the accumulated plastic strain $\tilde{p}$, which increases with load. Hence the plasticity is completely irreversible. Using a hardening law exponent α and the coefficient β, the function for the yield limit follows to:

$$\bar{\sigma}_y(\tilde{p}) = \beta \cdot (\tilde{p})^\alpha \tag{2.12}$$

By combining the models described, the plastic behaviour of a transversally isotropic material can therefore be described with only three parameters. These parameters can be determined with off-axis tensile tests as shown in [23], [31] and [33]. Due to its simplicity the model was adopted from different authors in their elastoplastic CDM-based models [2, 24, 31] and also finds application in this work.

2.3. Damage initiation and propagation using Cuntze's Failure Mode Concept

In order to predict discrete damage, like fibre- and interfibre failure, at the ply level, a suitable failure theory has to be incorporated in the model. Within the framework of the WWFE-II the predictive capabilities of 3D failure criteria for FRPs were compared [27]. The WWFE-II identified the FMC by Cuntze [28] as one of the criteria with a high predictive performance. In addition to the FMC, the Action Plane Strength Criterion (APSC) originally formulated by Puck and adapted by Deuschle also shows high capabilities [34, 35]. However, the APSC requires an additional algorithm to determine the angle of fracture respectively the plane of the potential interfibre fracture. Due to this, Cuntze's FMC is the main failure theory used in this work and will be briefly discussed in the following. Puck's APSC is implemented for comparison and described in the next section.

The FMC is characterised by the basic idea of separating failure modes. According to the FMC, a failure mode describes a certain failure mechanism. Each failure mechanism is covered by an individual failure criterion, which in turn is associated with only one material strength. For each of the failure modes an individual material stressing effort E_{ff} is calculated. This stressing effort is defined as the inverse of the stress-based reserve factor f_{res} [36]. The interaction of these different modes finally provides the global material stressing effort in the form of a sum equation [37]. Five different failure modes are distinguished.

Like the criteria of Hashin [7] or the APSC [35], Cuntze's FMC also differentiates fibre failure (FF) and interfibre failure (IFF). These modes are further distinguished according to the state of stress that causes failure. Thus, for FF two modes, which originate from tensile (FF1) and compressive (FF2) stresses exist. Three IFF modes are caused by tension (IFF1), compression (IFF2) and shear (IFF3) loading. The version of the FMC used in this work is published in [38]:

$$FF1 : Eff^{\|\sigma} = \sigma_{eq}^{\|\sigma} / R_{\|}^{t} \tag{2.13}$$

$$\text{with } \sigma_{eq}^{\|\sigma} = \sigma_1$$

$$FF2 : Eff^{\|\tau} = \sigma_{eq}^{\|\tau} / R_{\|}^{c} \tag{2.14}$$

$$\text{with } \sigma_{eq}^{\|\tau} = \sigma_1$$

$$IFF1 : Eff^{\perp\sigma} = \sigma_{eq}^{\perp\sigma} / R_{\perp}^{t} \tag{2.15}$$

$$\text{with } \sigma_{eq}^{\perp\sigma} = \left[(\sigma_2 + \sigma_3) + \sqrt{(\sigma_2 + \sigma_3)^2 + 4\tau_{23}^2}\right]$$

$$IFF2 : Eff^{\perp\tau} = \sigma_{eq}^{\perp\tau} / R_{\perp}^{c} \tag{2.16}$$

$$\text{with } \sigma_{eq}^{\perp\tau} = \left[b_{\perp\perp} \cdot \sqrt{(\sigma_2 + \sigma_3)^2 + 4\tau_{23}^2} + (b_{\perp\perp} - 1) \cdot (\sigma_2 + \sigma_3)\right]$$

$$IFF3 : Eff^{\perp\|} = \sigma_{eq}^{\perp\|} / R_{\perp\|} \tag{2.17}$$

$$\text{with}$$

$$\sigma_{eq}^{\perp\|} / R_{\perp\|} = \left(\left[\sqrt{b_{\perp\|}^2 \cdot I_{23-5}^2 + 4 \cdot R_{\perp\|}^2 \cdot (\tau_{13}^2 + \tau_{12}^2)^2} + b_{\perp\|} \cdot I_{23-5}\right] / (2 \cdot R_{\perp\|}^3)\right)^{\frac{1}{2}}$$

$$\text{and } I_{23-5} = 2\sigma_2 \cdot \tau_{12}^2 + 2\sigma_3 \cdot \tau_{13}^2 + 4\tau_{23}\tau_{13}\tau_{12}$$

The various failure modes can be combined to form a global criterion for failure in laminates. The interaction of the individual failure modes to a global material stressing effort Eff^m is described with the interaction exponent m. This parameter m interacts the single failure modes based on probabilistics. The global material effort Eff^m results in:

$$Eff^m = \sum_1^5 Eff^{mode} = \left(\frac{\sigma_{eq}^{\perp\sigma}}{R_\perp^t}\right)^m + \left(\frac{\sigma_{eq}^{\parallel\tau}}{R_\parallel^c}\right)^m + \left(\frac{\sigma_{eq}^{\perp\sigma}}{R_\perp^t}\right)^m + \left(\frac{\sigma_{eq}^{\perp\tau}}{R_\perp^c}\right)^m + \left(\frac{\sigma_{eq}^{\perp\parallel}}{R_{\perp\parallel}}\right)^m \tag{2.18}$$

As can be seen from the equations of the individual failure modes, no fracture angle is included because the stress invariants do not change with rotation or other transformation of the coordinate system. For this reason, the iterative search for the fracture angle, as it is necessary in the APSC, is not required. This increases the computational efficiency of the FMC compared to the APSC. If the global material stressing effort determined with the FMC reaches 1 at an integration point, further loading will cause a degradation of the material stiffnesses. Hence, a gradual damage development is activated at the integration point under consideration. First, the stiffnesses associated with the failure mode, which has the highest single effort, are degraded. As soon as further individual efforts reach one, the corresponding stiffnesses are also degraded. The assignment of the failure modes to the stiffnesses can be found in Tab. 1.

Table 1: Assignment of failure modes to damage variables

Failure mode	$FF1$	$FF2$	$IFF1$	$IFF2$	$IFF3$
Damage variable	d_{ft}	d_{fc}	d_{mt}	d_{mc}	d_s

Many degradation models in literature control the damage progression with the evolution of the failure indices of the damage initiation criteria [2, 9, 10, 11, 24]. Since most failure criteria are stress-based, which is also recommended by Rohwer [39], the development of damage is also indirectly stress-based. If, as in this work, the plasticity of the material is taken into account, the maximum effective stresses, apart from $\tilde{\sigma}_{11}$, are limited by the yielding of the material.

This also limits the damage variables. On this account the evolution of the damage variables is controlled by displacement in this work.

As soon as damage occurs in the fibre composite, the strain is no longer distributed smoothly, but varies in local areas. Characteristically, the strain increment is then localised in a small zone due to local damage, while the strain in the major part of the structure is diminishing [40]. Numerical models to describe failure behaviour must correctly reflect the energy dissipated in the fracture process zone. This is not the case in standard FE theory. As shown by Jirásek [41], the dissipated energy decreases with a refinement of the mesh to very small values. This results in a strong mesh dependency of the solution. In particular, smaller element sizes do not necessarily lead to a better converged solution. To remedy this, the crack band model of Bažant and Oh [42] is used. With this approach, the computed dissipated energy is regularised using a characteristic length of the finite element L_c:

$$g_M = \frac{G_M}{L_c} \text{ with } M \in \{ft, fc, mt, mc, s\} \tag{2.19}$$

In this equation G_M is the fracture toughness in the mode M and g_M is the dissipated energy per unit volume. As can be seen in sections 4.2 and 4.4.1 this approach cannot completely resolve the mesh dependency, but significantly mitigates it and is straightforward to implement. Therefore, it is used in several other damage descriptions proposed for composites [2, 26] and also in this work. To this end, the strain-controlled degradation model with crack band approach from Lapczyk and Hurtado [26] is adapted for use with the FMC. Each damage variable is calculated with the following equation:

$$d_M = \frac{\delta^f_{M,eq}(\delta_{M,eq} - \delta^0_{M,eq})}{\delta_{M,eq}(\delta^f_{M,eq} - \delta^0_{M,eq})} \text{ with } \delta^0_{M,eq} \leq \delta_{M,eq} \leq \delta^f_{M,eq} \tag{2.20}$$

The equivalent strain $\delta^0_{M,eq}$ describes the initiation of damage with the relationship:

$$\delta^0_{M,eq} = \frac{\varepsilon^0_M}{L_c} \tag{2.21}$$

Where L_c is the characteristic element length of the element under consideration. The equivalent strain at total failure $\delta^f_{M,eq}$ which corresponds to $d_M = 1$ is calculated with:

$$\delta^f_{M,eq} = \frac{2G_M}{\sigma^0_M L_c} \tag{2.22}$$

The stresses and strains at damage initiation (σ^0_M and ε^0_M) are not known a priori in Cuntze's FMC. Therefore, these measures are saved in the material routine during runtime when damage is initiated. In the interfibre failure modes damage can be caused by multiple stress components. In this case the component with the highest stress is used to control the degradation.

2.4. Damage initiation and propagation using Puck's Action Plane Strength Criterion

A version of the proposed material model with Puck‘s failure theory is used to compare it to Cuntze's FMC. At this point the theory of Puck will be discussed only briefly. For detailed information see [12] and [43]. In this work the theory described in VDI 2014 [44] is adopted. In Puck's APSC two stressing efforts are calculated. One effort for fibre failure $f_{E(FF)}$ and one for interfibre failure $f_{E(IFF)}$. Taking into account the strength in fibre direction in tension $R^t_{\|}$ and compression $R^c_{\|}$, the former is calculated with the following equations:

$$f_{E(FF)} = \frac{\tilde{\sigma}_{11}}{R^t_{\|}} \tag{2.23}$$

$$f_{E(FF)} = \frac{\tilde{\sigma}_{11}}{-R^c_{\|}} \tag{2.24}$$

The equations providing the stressing effort for interfibre failure $f_{E(IFF)}$ require stresses transformed to the action plane as an input. The orientation of the action plane, in other words the fracture angle Θ, is not known a priori. For this reason, fracture angles from $-90°$ to $+90°$ are iterated in $1°$ steps in the present implementation. The actual fracture plane is characterised by the highest stressing effort. For further calculations, the angle Θ that results in the highest stressing effort as well as the corresponding effort $f_{E(IFF)}(\Theta)$ is used.

The equations for $f_{E(IFF)}$ are the following:

$$f_{E(IFF)}(\Theta) = \sqrt{\left[\left(\frac{1}{R^t_{\perp}} - \frac{p^t_{\perp\Psi}}{R^A_{\perp\Psi}}\right)\sigma_n\right]^2 + \left(\frac{\tau_{nt}}{R^A_{\perp\perp}}\right)^2 + \left(\frac{\tau_{n1}}{R_{\perp\parallel}}\right)^2} + \frac{p^t_{\perp\Psi}}{R^A_{\perp\Psi}}\sigma_n \tag{2.25}$$

$$f_{E(IFF)}(\Theta) = \sqrt{\left(\frac{\tau_{nt}}{R^A_{\perp\perp}}\right)^2 + \left(\frac{\tau_{n1}}{R_{\perp\parallel}}\right)^2 + \left(\frac{p^c_{\perp\Psi}}{R^A_{\perp\Psi}}\sigma_n\right)^2} + \frac{p^c_{\perp\Psi}}{R^A_{\perp\Psi}}\sigma_n \tag{2.26}$$

For tensile stresses normal to the action plane the former equation is evaluated and otherwise the latter. The variables used are defined as follows:

$$\frac{p^t_{\perp\Psi}}{R^A_{\perp\Psi}} = \frac{p^t_{\perp\perp}}{R^A_{\perp\perp}} cos^2\Psi + \frac{p^t_{\perp\parallel}}{R_{\perp\parallel}} sin^2\Psi \tag{2.27}$$

$$\frac{p^c_{\perp\Psi}}{R^A_{\perp\Psi}} = \frac{p^c_{\perp\perp}}{R^A_{\perp\perp}} cos^2\Psi + \frac{p^c_{\perp\parallel}}{R_{\perp\parallel}} sin^2\Psi \tag{2.28}$$

$$cos^2\Psi = 1 - sin^2\Psi = \frac{\tau^2_{nt}}{\tau^2_{nt} + \tau^2_{n1}} \tag{2.29}$$

$$R^A_{\perp\perp} = \frac{R^c_{\perp}}{2(1 + p^c_{\perp\perp)}} \tag{2.30}$$

The variables $p^t_{\perp\parallel}$, $p^c_{\perp\parallel}$, $p^t_{\perp\perp}$ and $p^c_{\perp\perp}$ contained in these equations are inclination parameters of the master fracture body in the $(\sigma_n, \tau_{nt}, \tau_{n1})$-space and the variable $R^A_{\perp\perp}$ is parallel to fibre strength on the action plane against fracture due to $\tau_{\perp\perp}$ stresses.

In this way the fracture angle and the stresses transformed to the fracture plane are obtained in addition to the material stressing effort. Unlike Cuntze's FMC, Puck's APSC does not differentiate directly between interfibre failures due to tensile, compressive and shear loads. For this reason, a methodology is required to define the portion of the interfibre failure modes. Deuschle [32] formulated an orientation impact degradation measure n considering the computed fracture angle Θ and an angle of a most direct impact Θ_{md} for the mode under consideration:

$$n = \left[\frac{1 - n_{min}}{2} \cdot cos[2(\Theta - \Theta_{md})]\right] + \frac{1}{2} + \frac{1}{2}n_{min} \tag{2.31}$$

In this equation n can take values between 0 and 1. The parameter n_{min} controls the least impact. Since no experimental results are available, the value is set to zero as proposed in the work of Deuschle [43]. Tab. 2 shows the values for Θ_{md} for the different components:

Table 2: Angles of most direct impact on the stiffness components

Θ_{md}	E_{22}	E_{33}	G_{12}	G_{13}	G_{23}
n_i	0°	90°	•	•	•
n_{ij}^{+}	•	•	0°	90°	+45°
n_{ij}^{-}	•	•	0°	90°	−45°

In the first step, a general damage variable for interfibre failure d_{IFF} controlled by the largest strain component is calculated. This general damage variable is then used to calculate the individual damage variables taking the orientation impact degradation measure into account:

$$d_i = n_i \cdot d_{IFF} \tag{2.32}$$

$$d_{ij} = n_{ij}^{+} \cdot d_{IFF} + n_{ij}^{-} \cdot d_{IFF} - n_{ij}^{+} \cdot d_{IFF} \cdot n_{ij}^{-} \cdot d_{IFF} \tag{2.33}$$

The other parts of the degradation model work as described for the FMC in section 2.3.

3. Numerical implementation

The suggested elastoplastic material model has been implemented in Abaqus / Standard as UMAT. The following section describes the implementation of the algorithms for updating the Cauchy nominal stresses, the state variables as well as the consistent tangent stiffness matrix. Both the implementation and the verification are shown considering the version of the material model with Cuntze's FMC.

3.1. Computational procedure

At the beginning of each increment the values ε_n^e, ε_n^p, $\Delta\varepsilon$, $\tilde{p}_n$, σ_n of the previous increment n are retrieved. Then the effective stress $\tilde{\sigma}$ at the time increment n is calculated with Eq. 2.1. With this information an elastic predictor consisting out of a trial strain $\varepsilon_{n+1}^{trial}$ and a trial stress σ_{n+1}^{trial} is determined. The trial stress is then used to check the yield criterion F, cf. Eq. 2.8. If the increment is elastic, the stresses and strains at time $n+1$ will be updated with the quantities of the elastic predictor. Otherwise, the actual effective stress vector $\tilde{\sigma}_{n+1}$ and the scalar valued accumulated plastic strain have to be found for the current increment. For this purpose, the effective stress vector $\tilde{\sigma}_{n+1}$ is expressed as a function of the trial stress vector $\tilde{\sigma}_{n+1}^{trial}$:

$$\tilde{\sigma}_{n+1} = (\boldsymbol{I} + \Delta\lambda \boldsymbol{D}^e \cdot \boldsymbol{M} \cdot \boldsymbol{P})^{-1} \cdot \tilde{\sigma}_{n+1}^{trial} \tag{3.1}$$

In this equation $\boldsymbol{I}$ is the identity matrix, $\Delta\lambda$ is the plastic multiplier and $\boldsymbol{D}^e$ is the elastic compliance matrix. The equivalent plastic strain of the increment $n+1$ can be determined with the following equation:

$$\tilde{p}_{n+1} = \tilde{p}_n + \Delta\lambda\sqrt{(\boldsymbol{P} \cdot \tilde{\sigma}_{n+1})^T : \boldsymbol{Z} : (\boldsymbol{P} \cdot \tilde{\sigma}_{n+1})} \tag{3.2}$$

Where $\boldsymbol{Z}$ is the mapping matrix:

$$\boldsymbol{Z} = \begin{bmatrix} 0 & 0 & 0 & 0 & 0 & 0 \\ & \frac{2}{3} & -\frac{1}{6} & 0 & 0 & 0 \\ & & \frac{2}{3} & 0 & 0 & 0 \\ & & & \frac{1}{3a} & 0 & 0 \\ & sym. & & & \frac{1}{3a} & 0 \\ & & & & & \frac{1}{6} \end{bmatrix} \tag{3.3}$$

A return mapping algorithm (RMA) is utilised to determine the only unknown variable in these equations $\Delta\lambda$. The RMA used in this work is described in [32] and was adapted by Din et al. [24] for the plastic potential as used by Sun and Chen [23]. The plastic multiplier determined with the RMA is used to correct the elastic predictor for the plastic effects. Regardless of whether the current increment is elastic or plastic in the next step of the procedure, the failure criterion, in this case Cuntze's FMC, is evaluated. If the total material stressing effort Eff^m is greater or equal than one, the damage variables d_{ft}, d_{fc}, d_{mt}, d_{mc} and d_s are updated. After this step the elastic and plastic strain components are calculated and the nominal stress vector σ_{n+1} is updated considering the updated damage variables. At the end of the routine, the state variables are returned and the consistent tangent stiffness matrix is determined with the procedure described in the next section. The calculation procedure for each increment at each integration point is shown in Fig. 2.

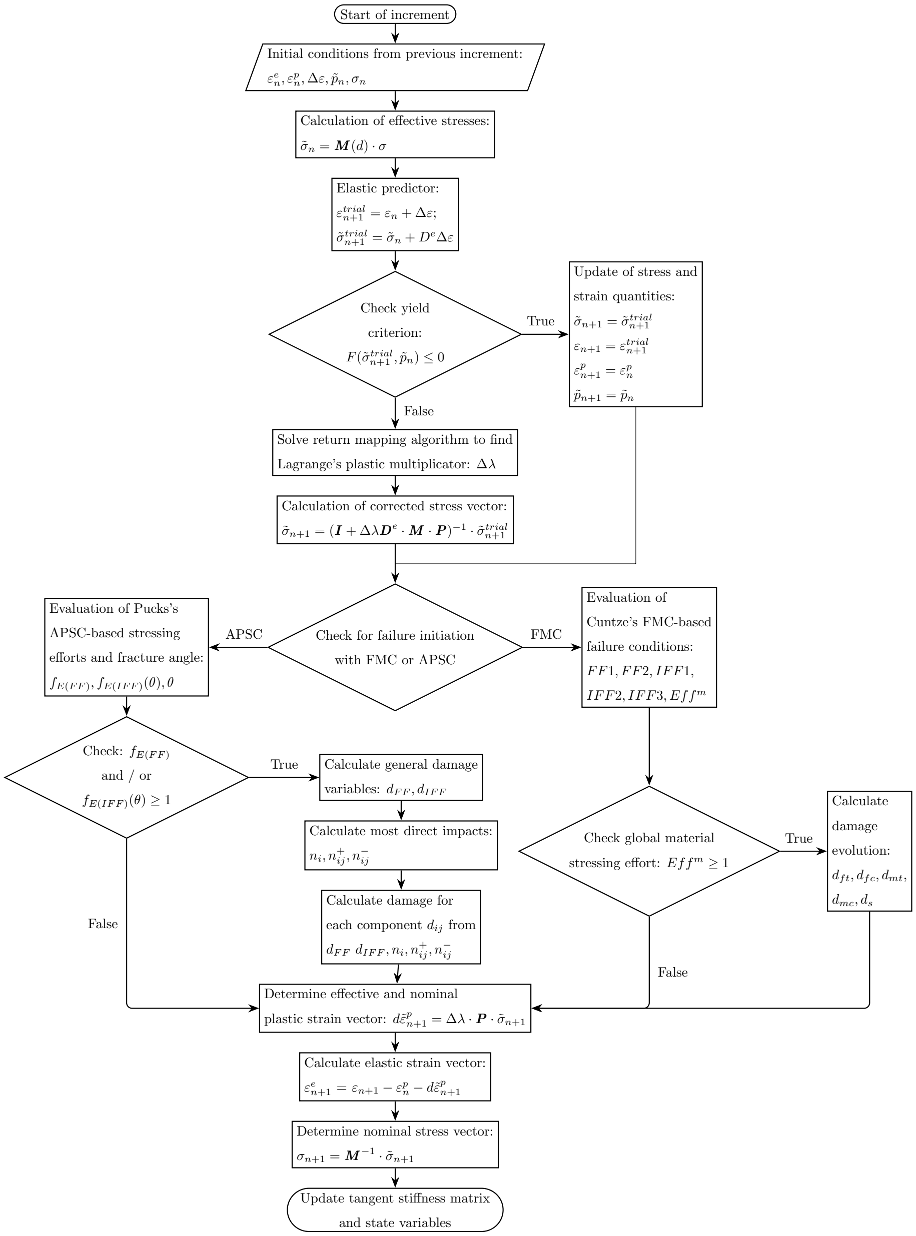

Figure 2: Algorithm flow chart of UMAT subroutine

3.2. Tangent stiffness matrix

Since the described material model is implemented for the implicit solver Abaqus / Standard, a tangent stiffness matrix, which is consistent to the stressupdate algorithm, is required. Din et al. [24] have derived the following operator to calculate the consistent tangent stiffness for the plasticity model of Sun and Chen [23] in combination with damage:

$$C^{ep} = \frac{\partial \Delta \tilde{\sigma}_{n+1}}{\partial \Delta \varepsilon_{n+1}^{trial}} = \left[(C_0)^{-1} + \Delta\lambda \boldsymbol{P} + \frac{1}{2\bar{\sigma}_y \tilde{H} \tilde{\zeta}} \boldsymbol{M} n_F n_F^T - \frac{\Delta\lambda}{\tilde{\zeta}^2} \boldsymbol{M} n_F n_F^T \boldsymbol{Z} \boldsymbol{P} \right]^{-1} \tag{3.4}$$

In this case $n_F = \boldsymbol{P} \cdot \tilde{\sigma}_{n+1}$, $\zeta = \sqrt{n_F^T \boldsymbol{Z} n_F}$, $\tilde{H} = \alpha\beta\tilde{p}_{n+1}^{\alpha-1}$ and $(C_0)^{-1}$ is the compliance matrix of the transversely isotropic material. In the present work, this operator was transferred to the three-dimensional stress state using the matrices $\boldsymbol{P}$ and $\boldsymbol{Z}$ specified in the sections 2.2 and 3.1. Tests of the implementation showed poor convergence at beginning of damage. Therefore, the operator 3.4 is only used as long as all damage variables d_I are equal to zero. In this case the matrix $\boldsymbol{M}$ is always the same as the identity matrix $\boldsymbol{I}$ and the operator becomes:

$$C^{ep} = \frac{\partial \Delta \tilde{\sigma}_{n+1}}{\partial \Delta \varepsilon_{n+1}^{trial}} = \left[(C_0)^{-1} + \Delta\lambda \boldsymbol{P} + \frac{1}{2\bar{\sigma}_y \tilde{H} \tilde{\zeta}} \boldsymbol{I} n_F n_F^T - \frac{\Delta\lambda}{\tilde{\zeta}^2} \boldsymbol{I} n_F n_F^T \boldsymbol{Z} \boldsymbol{P} \right]^{-1} \tag{3.5}$$

From the beginning of damage on, the tangent stiffness matrix is numerically determined using the perturbation technique, which is based on forward difference approximation. The components of C^{ep} are calculated as [45]:

$$C_{ijkl}^{ep} = \frac{d\sigma_{ij}}{d\varepsilon_{kl}} \approx \frac{\sigma_{ij}(\hat{\varepsilon}^{kl}) - \sigma_{ij}(\varepsilon)}{\Delta\varepsilon}, \text{ with } \hat{\varepsilon}^{kl} = \varepsilon + \Delta\varepsilon^{kl} \tag{3.6}$$

Here $\Delta\varepsilon^{kl}$ is the perturbation strain for the kl-component and $\hat{\varepsilon}^{kl}$ is the corresponding perturbed strain vector.

3.3. Viscous regularisation

With implicit solvers the degradation of stiffness sometimes lead to convergence problems. The reason for this is a no longer positive definite tangent stiffness matrix. To mitigate this problem, Lapczyk and Hurtado [26] have proposed the introduction of an artificial viscosity based on the regularisation model of Duvaut and Lions [46] according to the following equation:

$$\dot{d}^v_M = \frac{1}{\eta_M}(d_M - d^v_M) \tag{3.7}$$

In this equation η_M describes the relaxation time of the viscous system and d^v_M is the regularised damage variable associated with mode I. The regularised damage variable for the increment $n+1$ is derived according to Chen et al. [2] as:

$$d^v_{M,n+1} = \frac{\Delta t}{\eta + \Delta t} d_{M,n+1} + \frac{\Delta t}{\eta + \Delta t} d^v_{M,n} \tag{3.8}$$

3.4. Characteristic and critical finite element size

For the crack band approach, described in section 2.3, the in-plane characteristic element length L_c is needed in order to scale the linear degradation behaviour to the element size. This length L_c for square elements is determined by Bažant and Oh [42] with the following relationship where A_{IP} is the in-plane area of the element:

$$L_c = \frac{\sqrt{A_{IP}}}{cos(\gamma)} \tag{3.9}$$

Here $|\gamma| \leq 45°$ is the angle of the mesh line at which the crack band propagates. For an unknown crack propagation direction Maimí et al. [47] showed that the average of Eq. 3.10 $\bar{L}_c = 1.12\sqrt{A_{IP}}$ can be used. The solver provides the characteristic element length $L_{c,ABQ}$ in the UMAT interface for solid elements as the cube root of the element volume. For hexahedral elements, which are used in the presented work, this value must be corrected with the following formula in order to obtain the in-plane element length, taking into account the ply respectively element thickness t and the unknown crack direction:

$$L_c = 1.12 \cdot \sqrt{\frac{L^3_{c,ABQ}}{t}} \tag{3.10}$$

The crack band approach assumes an element-wide crack band and adjusts the degraded modulus to ensure that the correct fracture energy is preserved for different element sizes. With this approach the element size has an upper bound L^*. This so-called critical element size is calculated using the pristine modulus E_M, the critical strain energy G_M and the strength X_M for each mode M [42]:

$$L^* = \frac{2E_M G_M}{X_M^2} \tag{3.11}$$

If larger elements are used, a softening modulus of $-\infty$ would be determined with the crack band approach. This would lead to a sudden stiffness drop. In practise Bažant and Oh [42] recommend an element size of about half the value determined for L^*.

4. Numerical results and discussion

To illustrate the applicability and effectiveness of the proposed combined elastoplastic damage model several numerical simulations of the progressive failure behaviour are performed. This section presents the results of three benchmark examples to verify the model. In addition, a $[\pm 45]_{2s}$ laminate under tensile loading was analysed. The validation is carried out with open-hole tension test specimens with a quasi isotropic (QI) ply stacking sequences. The failure theories from Puck and Cuntze are also being compared and discussed on this basis.

4.1. Material and model parameters

Unless otherwise stated, all of the simulations have been performed with the thermoplastic fibre composite material AS4/PEEK using the material and model parameters listed in Tab. 3. The elastic as well as the plastic properties are adopted from Sun and Yoon [33]. The values for tensile and shear strengths are taken from Kawai [48] whereas the compressive strengths are obtained from Sun and Rui [49]. The values for the critical strain energies are adopted from Carlile et al. [50] and Chen et al. [2]. Since the required parameters for Cuntze's FMC were not available for AS4/PEEK, the values determined by Petersen et al. [38] for M21/T700GC, a material with a tough epoxy matrix, were used.

Table 3: Material properties and model parameters for AS4/PEEK

E_{11}	$E_{22} = E_{33}$	$G_{12} = G_{13}$	G_{23}	$\nu_{12} = \nu_{13}$	ν_{23}
126.7 GPa	10.3 GPa	6.0 GPa	3.45 GPa	0.32	0.49
$R^t_{\parallel}$	$R^c_{\parallel}$	$R^t_{\perp}$	$R^c_{\perp}$	$R_{\perp\parallel}$	η
2023.0 MPa	1234.0 MPa	92.7 MPa	176.0 MPa	82.6 MPa	0.0002
$G_{ft} = G_{fc}$	$G_{mt} = G_{mc}$	G_s	a	α	β
128.0 N/mm	5.6 N/mm	4.93 N/mm	1.5	0.142857	295.0274

The parameters are listed in Tab. 4. The parameters for the APSC by Puck were chosen according to Puck et al. [51], cf. Tab. 4.

Table 4: Parameters for FMC and APSC

FMC	$b_{\perp\parallel}$	$b_{\perp\perp}$	m		
	0.44	1.266	2.6		
APSC	$p^t_{\perp\parallel}$	$p^c_{\perp\parallel}$	$p^t_{\perp\perp}$	$p^c_{\perp\perp}$	$m = s$
	0.35	0.30	0.30	0.30	0.5

4.2. Verification with representative volume elements and periodic boundary conditions

This subsection is concerned with the verification of the proposed anisotropic elastoplastic damage model. The benchmark examples are calculated with cubic single element models with side lengths of 1 mm using reduced integrated solid elements (C3D8R). The time step in the simulations is determined automatically with the restriction that the maximum time step is set to 0.005. The support and the load application are realised with periodic boundary conditions to be able to apply a load in one specific direction. These periodicity conditions are achieved by linking the degrees of freedom of the cubic model node-to-node as well as to reference points. This is done by using a plug-in for Abaqus CAE called EasyPBC by Omairey et al. [52]. As an example in Fig. 6 a single element model with a pure loading in the 12-direction is shown. In this case, the element nodes C1, C4, C5 and C8 are coupled with the reference point RP-1, for instance.

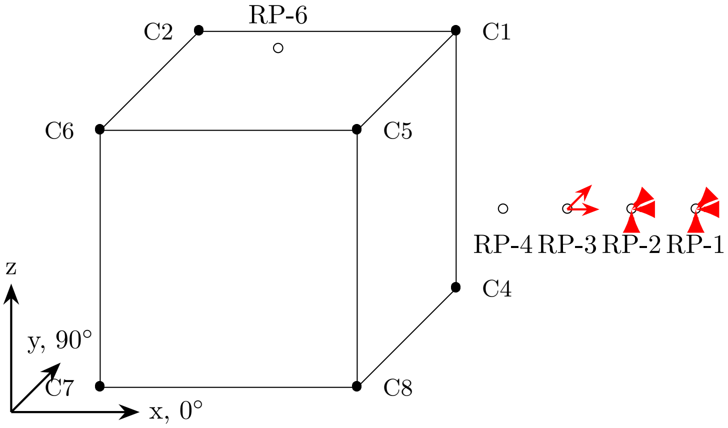

Figure 3: Single element model with periodic boundary conditions with loading in 12-direction

The first benchmark assesses the material model under cyclic tensile-compressive loading in fibre direction. The resulting stress-strain curve is shown in Fig. 4. In this verification the cube is discretised with one element. The model is first loaded in tension beyond initial failure (1). After that, the cube is unloaded (2) and then loaded in compression beyond initial compression failure (3). Once unloaded again (4), the cube is subjected to tensile loads of up to 3 % strain and significant damage (5). It can be seen that the damage accumulated in the tensile part is accounted for in the compressive part of the cycle. Vice versa the compressive damage is considered in the second tensile loading cycle. This behaviour is in line with the expectations since the damage variables d_{ft} and d_{fc} are combined with Eq. 2.4 to a total damage variable in fibre direction d_f.

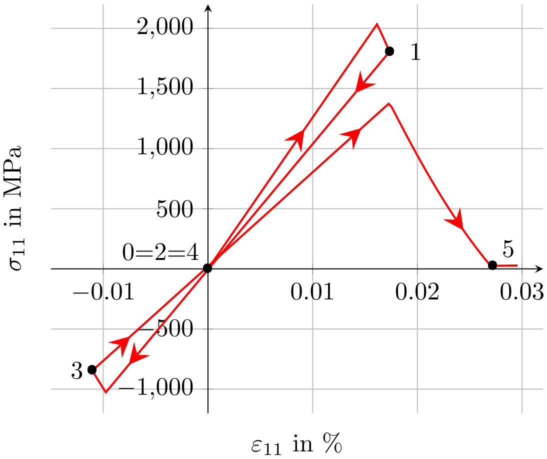

Figure 4: Load displacement curves under uniaxial tensile-compressive cycling load in fibre direction

In the second benchmark example, cf. stress-strain curves in Fig. 5, a cube is subjected to a tensile load transverse to the fibre direction. Four different meshes were tested to assess the mesh dependency. Three models have a regular mesh with one, 27 and 125 elements. The fourth model is also discretised with 27 elements, but with an irregular mesh. In addition, the models with the regular meshes were also calculated with the crack band approach switched off. It can be observed that the stress-strain curves from the models with the crack band approach show some deviations, but compared to the models without the approach a significant improvement is achieved. It can therefore be concluded that the crack band approach fulfils its purpose. In addition, it can be seen that the material shows some plasticity over 0.5 % strain in the transverse direction.

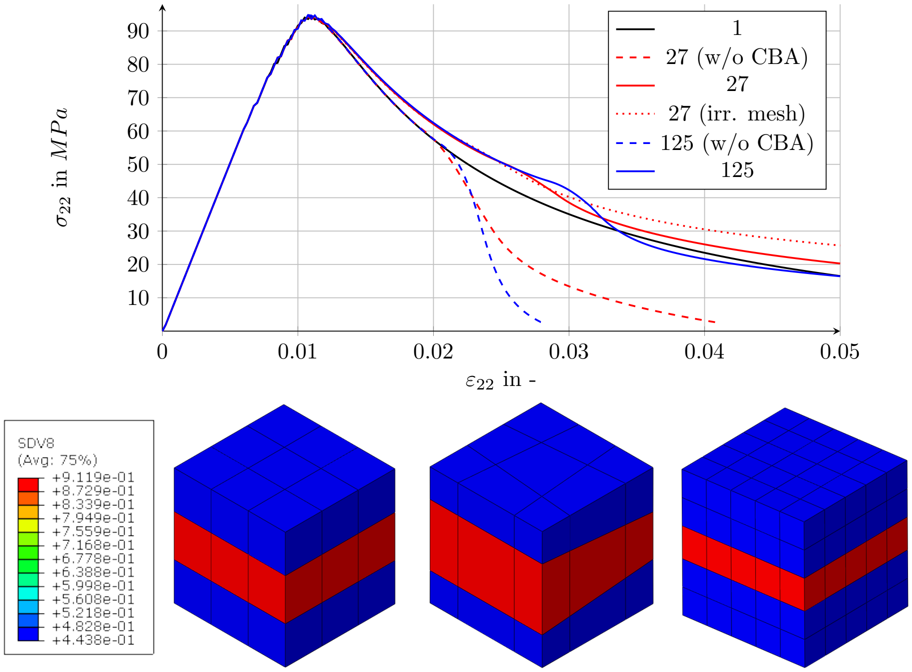

(a) 27 (b) 27 (irr. mesh) (c) 125

Figure 5: Stress-strain curve of a cubic model subjected to transverse tension loading and discretised with different meshes

The third benchmark example considers a cubic model, shown in Fig. 6, again with periodic boundary conditions, subjected to pure shear loading in the 12-direction. The cube is loaded up to a certain point and unloaded again until it is stress-free. This cycle is repeated up to total failure at 8 % shear strain. The resulting stress-strain curve is plotted in Fig. 6. It can be seen that the plastic strain is taken into account when the load is relieved. Besides that, the point of the previous loading is reached again when the element is reloaded. After the strength has been exceeded, the loading and unloading takes place with the degraded shear modulus.

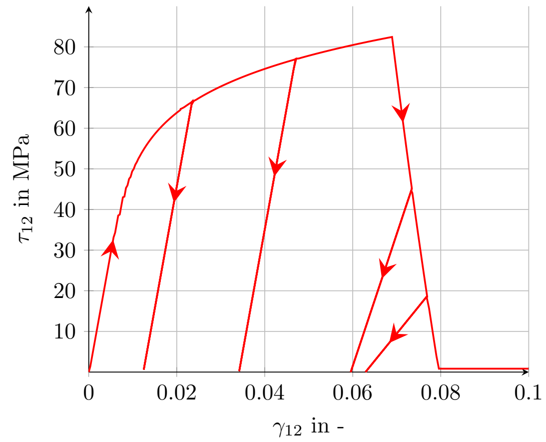

Figure 6: Stress-strain curve of a cubic model subjected to cyclic in-plane shear loading

For all three benchmark examples, it can be stated that the maximum stress, before degradation begins, corresponds to the specified strengths.

In order to assess the interaction of stresses, test case 2 of the WWFE-II was adopted. First, the cubic model discretised with one element was loaded with different magnitudes of hydrostatic pressure p_{hyd} and then in a second step subjected to a shear loading until failure. The resulting stresses at failure are plotted in Fig. 7. Since no experimental data are available for the material used in this work, only a qualitative comparison with results from WWFE-II can be made. Nevertheless, the calculations in this work are consistent with the observations in WWFE-II, as the hydrostatic stresses have an influence on the shear stress on failure. As the hydrostatic stress decreases, the shear stress at failure increases.

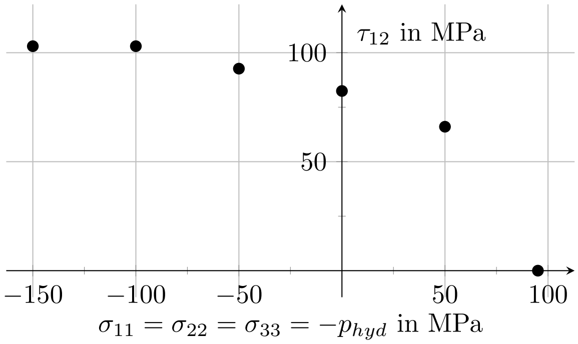

Figure 7: Fracture stress τ_{12} vs. stress $p_{hyd}(= -\sigma_{11} = \sigma_{22} = -\sigma_{33})$ following WWFE-II Test Case 2

4.3. Numerical results of AS4/PEEK $[\pm 45°]_{2s}$ *laminates*

To demonstrate the capabilities of the model in terms of plasticity and damage modelling a tensile test, reported in literature, of a AS4/PEEK $[\pm 45°]_{2s}$ laminate is numerically analysed. The test coupon of Lafarie-Frenot and Touchard's [17] experiment has the dimensions 230 mm x 20 mm x 1 mm. In the numerical analysis the laminate is modelled with eight stacked elements, where each ply consists of one C3D8R element. The thickness of the model is with 1 mm equal to the experiment. The other two dimensions are also 1 mm. Using periodic boundary conditions, the model behaves like a representative volume of the test specimen. The model is shown in Fig. 8.

In Fig. 9 the stress-strain curves of the experimental test as well as the curve generated by the presented model are plotted. It can be observed that the elastoplastic material model is able to reproduce the experimental behaviour very well. For comparison, the same model was calculated with a variant of the presented material model without plasticity. While the predicted strength is comparable, the elongation at failure is clearly too low.

4.4. Progressive damage analyses of open-hole tension specimens

In this subsection the capabilities of the proposed elastoplastic / damage model are demonstrated. For this, the material model is used to analyse the

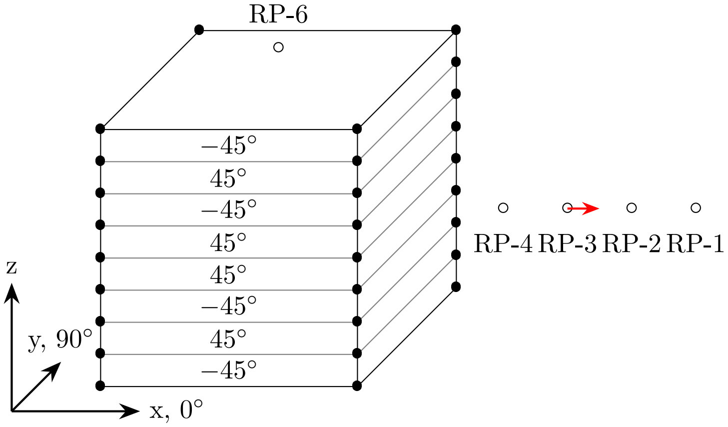

Figure 8: Finite element model of AS4/PEEK $[\pm 45°]_{2s}$ tensile test with periodic boundary conditions

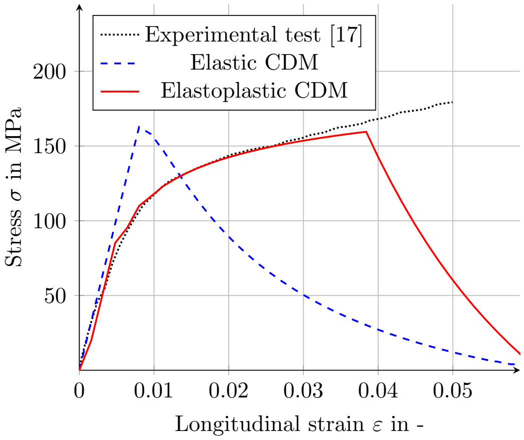

Figure 9: Experimentally and numerically determined stress-strain curves of an AS4/PEEK $[\pm 45°]_{2s}$ tensile test

progressive failure of AS4/PEEK open-hole tension specimens with a quasi-isotropic $[0/45/90/-45]_{2s}$-layup and different geometries. The experimental results are taken from [53]. In addition, the failure behaviour of the specimens is also predicted with the APSC failure criterion by Puck. On this basis, a comparison in terms of prediction accuracy and computation time between the two failure criteria used in combination with the proposed model is performed. Girão Coelho et al. [54] state that symmetry can be used to reduce the simulation expense, but not in the loading direction, since the restraining conditions may change the stress field. Therefore, all simulations are performed modelling 1/4 of the specimens. The geometry and boundary conditions of the model are shown in Fig. 10. The open-hole tension specimens are loaded with a displacement load applied to one end. The time step is limited to a maximum value of 0.02.

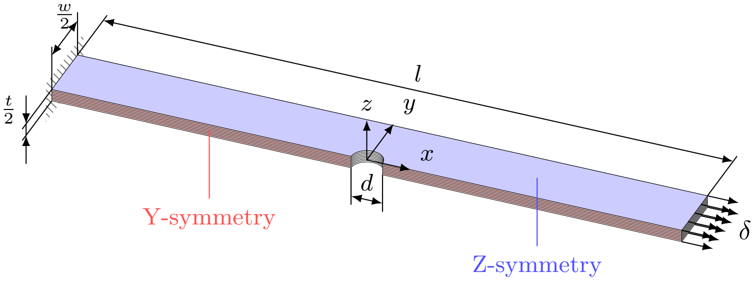

Figure 10: Sketch of model geometry and boundary conditions

4.4.1. Element type and size

In order to save computation time and minimise the tendency for shear locking reduced integrated linear solid elements (C3D8R) are used. The element size must be chosen in a way that the premise of the crack band approach is complied: The band width, where the damage localises in, is equivalent to the element dimension. Elements sized larger than the damage process zone would lead to a local snap back. Using the crack band approach with elements that are too small would lead to an incorrect stress field. With Eq. 3.11 the maximum element size $L^* = 1.56$ mm is determined. Bǎzant and Oh [42] recommend using an element size of about half the value calculated for L^*. In the case of the material parameter used for AS4/PEEK this leads to an element size of 0.78 mm. In order to check the determined element size a strength prediction study with different meshes from 0.5 mm to 1.0 mm was performed. In through-thickness direction every ply is discretised by one element and the element edges are not aligned with ply orientation. The specimen considered for this purpose has the dimension $l = 100$ mm, $w = 20$ mm, $t = 2$ mm and $d = 5$ mm. The results of the study are shown in Tab. 5.

Table 5: Comparison between strength prediction of open hole tension specimen with 5 mm hole diameter with different meshes and experiment (15.514 kN).

In-plane edge length mm	Predicted strength kN	Deviation to experiment %
0.500	14.455	−5.58
0.625	15.589	1.82
0.750	15.598	1.88
0.780	15.451	0.92
0.875	15.137	−1.13
1.000	16.903	+10.40

The results show that a small element size leads to an underestimation whereas a too large element size leads to an significant overestimation of the failure load. With less than 2 % the deviation between experiment and numerical analysis is small for element sizes in the range of the recommended element size of 0.780 mm. The deviation is with -0.92 % the smallest for the previously determined element size of 0.780 mm. Therefore, when using the material model in combination with the crack band approach, it is recommended that the element size used is based on that recommended by Bǎzant and Oh. Consequently, this element size is also used for all analyses in this work. Unfortunately, Maa and Cheng do not give the standard deviation for the experimental results in [53].

4.4.2. Stiffness comparison between experimental and numerical gained load displacement curve

In the experimental campaign of Maa und Cheng [53] a clip gauge with a blade spacing of $E = 30$ mm was mounted in the middle of the specimens. The resulting load-displacement curve for one specimen ($l = 100$ mm, $w = 20$ mm, $t = 2$ mm and $d = 5$ mm), cf. Fig. 11, is used to perform a comparison between experiment and numerical prediction with the proposed material model. It can be seen that the stiffness of the specimen is well reproduced by the model. However, a slightly larger deviation occurs after about 0.1 mm applied displacement and the numerical simulation overestimates stiffness in the experiments by 5.5 %.

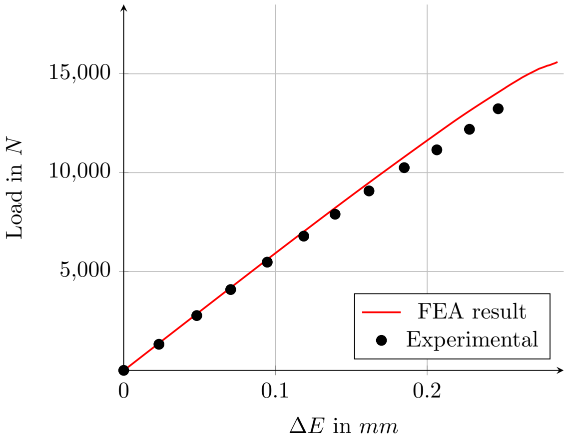

Figure 11: Comparison between the calculated and the measured clip gauge load-displacement curve for an open-hole tension specimen (AS4/PEEK, $l = 100$ mm, $w = 20$ mm, $t = 2$ mm and $d = 5$ mm)

4.4.3. Strength prediction of specimens with $[0/45/90/-45]_{2s}$*-layup*

Strength predictions for ten different open-hole tension specimens varying in geometry were performed with the proposed material model using Cuntze's FMC as well as using the APSC by Puck. Two series of specimens, which differ in the width w, were investigated. For the series with a specimen width of 20 mm as well as for the series with a width of 30 mm, five specimens with hole diameter to width ratios d/w between 0.1 and 0.5 were analysed. The analyses were terminated when a load drop of at least 25 % occurred. In Tab. 6 the experimentally determined as well as the numerically predicted strengths are summarised. In addition, the differences between experiment and analysis is also stated in Tab. 6.

Table 6: Comparison of strength predictions for OHT specimens with experimental results from Maa and Cheng [53] (thickness $t = 2$ mm, length $l = 100$ mm)

				Cuntze's FMC		Puck's APSC	
w	d	d/w	Experiment [53]	Prediction	Diff.	Prediction	Diff.
mm	mm	•	kN	kN	%	kN	%
•	2	0.10	22.98	22.10	-3.84	23.47	2.11
•	3	0.15	19.31	19.26	-0.27	20.60	6.69
20	5	0.25	15.31	15.35	0.28	17.28	12.85
•	8	0.40	11.67	11.64	-0.30	12.30	5.42
•	10	0.50	9.22	9.71	5.28	10.25*	11.19*
•	3	0.10	30.62	30.34	-0.91	32.21	5.18
•	6	0.15	24.06	22.17	-7.85	24.21	0.62
30	10	0.25	18.51	17.94	-3.11	17.89	-3.35
•	12	0.40	17.87	16.58	-7.21	17.58*	-1.61*
•	15	0.50	14.16	13.47	-4.87	13.89	-1.92

The deviation of the predicted strength of the series with 20 mm width using the FMC lies between -3.84 % and 5.28 %. Compared to this, the interval of the deviation when using the APSC is with a difference between 2.11 % and 12.85 % a little larger. It must be noted that for the specimens marked with * no convergence could be obtained with the standard settings described in section 4.1. Nevertheless, to get a solution, the value η for the viscous regularisation was set to 0.002. This may cause the determined failure loads to be higher than with the default settings and may explain the relatively high deviation of 11.19 % of the specimen with 10 mm hole diameter compared to the other results. The deviation of the prediction using Cuntze's FMC of the second series with a width of 30 mm is slightly higher compared to the first, but the intervall of the deviations is nearly the same. The differences are between -7.85 % and -0.91 %. With deviations ranging from -3.35 % to 5.18 % the prediction accuracy of the APSC-based prediction is comparable to the results obtained with the FMC. In general, it can be said that all analyses provide a satisfactory deviation between the predicted and experimentally determined failure loads. In addition, it can be deduced that the FMC usually underestimates the failure load, while the APSC tends to overestimate the failure strength.

The structural behaviour of the first series ($w = 20$ mm) of experiments was also predicted by several other authors. An overview is given in Tab. 7. For example Chen et al. [2] use the same plasticity model but combined with the failure criterion of Hashin and continuum shell elements. Their prediction is afflicted with errors between -5.8 % and $+14.8$ %. However, unlike the prediction with the model proposed in this work, there is a dependency of the error to the d/w ratio. For low values of d/w the failure load is underestimated and for high values it is overestimated. The same trend can be observed in the prediction of Maa and Cheng [53], who originally performed the experimental study. They use two different versions of a continuum damage model with their own failure criterion and a non-linear Ramberg-Osgood relationship to model the non-linear behaviour in shear combined with reduced integrated plane-stress shell elements. The second models of Maa and Cheng [53] contains a modified fibre failure criterion.

Table 7: Comparison of predicted failure loads from different FE analyses

d in mm	Error in %				
•	Present		Chen et al. [2]	Maa and Cheng [53]	
•	FMC	APSC	•	Model 1	Model 2
2	-3.84	2.11	-5.79	-15.25	-5.61
3	-0.27	6.69	-6.15	-41.67	-8.60
5	-0.28	12.85	7.33	-27.58	0.20
8	0.30	5.42	12.30	-16.00	6.77
10	5.28	11.19	14.77	-6.34	16.81

In summary, the strength prediction of the open-hole tension specimens using the proposed material model in combination with Cuntze's FMC as well as Puck's APSC is fairly accurate, especially when compared to other predictions. Parts of the deviation could be attributed to the fact that the parameters of the FMC as well as of the APSC were not determined for the considered material.

4.5. Predicted load-displacement curves

Fig. 12 shows the resulting load-displacement curves for the series with a width of $w = 20$ mm and the FMC-based material model. It can be observed that the predicted stiffnesses of the various test specimens are initially almost identical. As the load increases, the difference between the stiffnesses becomes larger. The larger the hole diameters are, the lower are the stiffnesses as the net cross section is reduced. The failure displacements behave in exactly the same way. Due to the lower failure load with larger hole diameters and a stiffness of the same magnitude, the displacement at failure is lower for large hole diameters. Two points are marked in the load-displacement curve of the specimen with a hole diameter of $d = 5$ mm. Point A indicates the damage progress at which the load-bearing capacity of the structure is no longer given. In addition, the point at which the analysis was aborted is marked as point B.

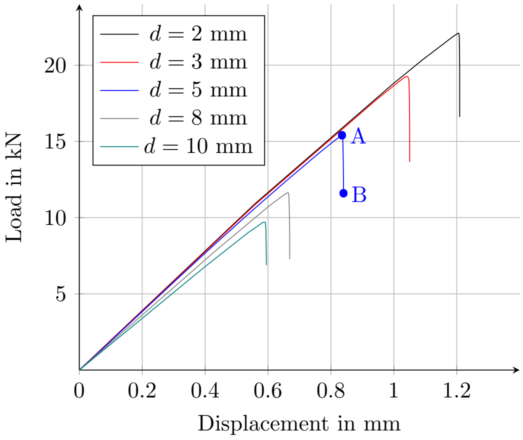

Figure 12: Load-displacement curves of AS4/PEEK $[0/45/90/-45]_{2s}$ open-hole tension specimens predicted with Cuntze's FMC

565 ### *4.5.1. Damage progression in open-hole tension specimen*

The fibre damage progression d_f in a 0°-ply of the specimen with 5 mm hole diameter is shown in Fig. 13 at the points A and B.

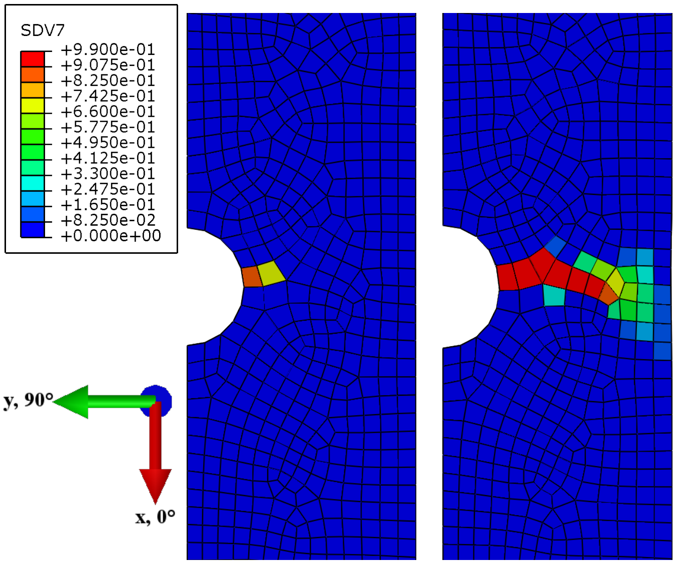

(a) d_f at A (b) d_f at B

Figure 13: Fibre damage evolution in a 0°-ply of open-hole tension specimen

It can be seen that the damage evolution is perpendicular to the fibre and loading direction x in a line starting from the middle of the specimen at the hole. The slightly curved shape of the damage path can be attributed to the disordered mesh. At the point of loss of load bearing capacity only three elements are damaged, whereas nearly the whole net section is damaged when the load has dropped to 75% of the failure load. Fig. 14 shows the transverse matrix damage evolution. At point A the transverse matrix damage d_m in a 90°-ply is concentrated around the hole in the specimen. No element is completely damaged at this stage. Further damage progression up to state B leads to x-shaped damage which is nearly symmetrical to the YZ plane. Fully damaged elements can be found in an area perpendicular to the loading direction, that is three times wider than the fibre damage area in the 0°-ply.

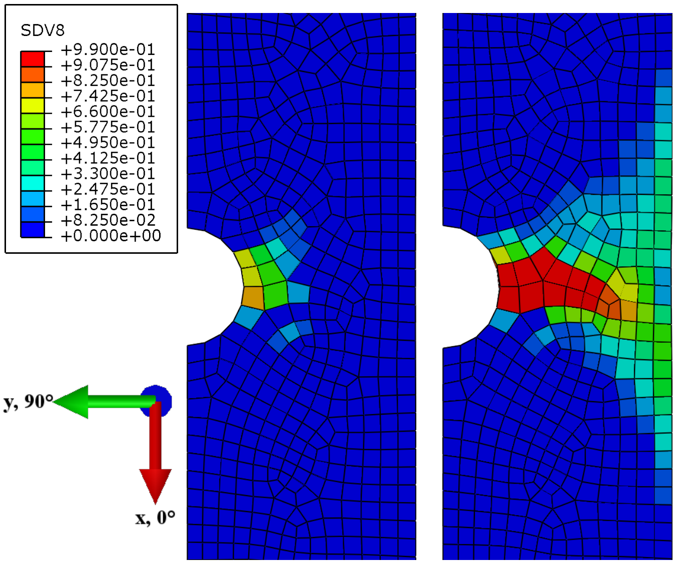

(a) d_m at A (b) d_m at B

Figure 14: Transverse matrix damage evolution in a 90°-ply of open-hole tension specimen

As can be seen in Fig. 15, the shear matrix damage progression d_s in a $-45°$-ply at point A is concentrated around the edge of the hole. No elements are totally damaged yet. During further loading up to point B the damage progresses towards the outer edge of the specimen. Different from the fibre and transverse matrix damage the damage growth is not perpendicular to the loading direction, but is perpendicular to the fibre direction of the −45°-ply.

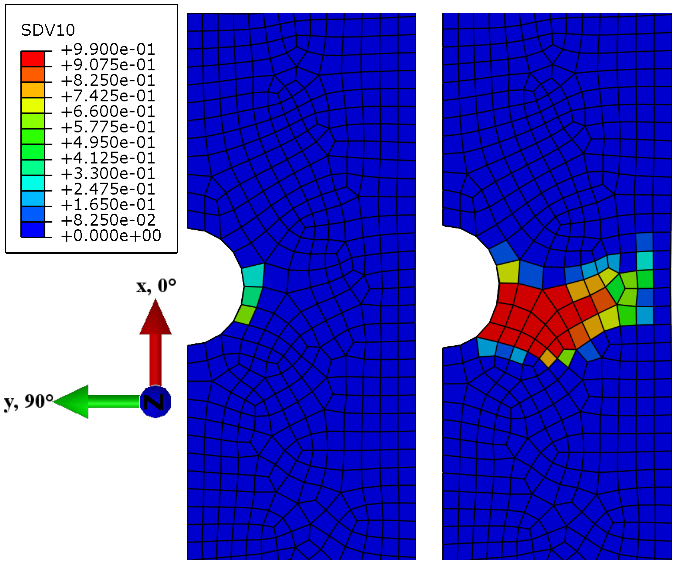

(a) d_s at A (b) d_s at B

Figure 15: Shear matrix damage evolution in a −45°-ply of open-hole tension specimen

The predicted intralaminar failure patterns using the proposed methodology are in line with the findings of other authors [10, 24], analysing open-hole tension specimens with a quasi-isotropic layup. For example, they also observed x-shaped transverse matrix cracks in the 90°-plies. The observed band of fibre failures perpendicular to the loading direction starting in the middle of the specimen from the edge of the hole leads to the expected net section failure mode. As reported in literature, this failure mode causes the total failure of the specimen in experiments [10]. The distinction between transversal matrix damage and those under shear load is not made in other studies as the failure criteria used, unlike the FMC, do not distinguish between the different modes of matrix failure.

4.5.2. Accumulated plastic strain in open-hole tension specimen

Fig. 16 shows the accumulated equivalent plastic strain $\tilde{p}$ in a 90°-ply and a −45°-ply of the specimen with a 20 mm width and 5mm hole diameter. It can be seen that the highest plastic strain in both cases is at the edge of the hole in the middle of the long side of the specimen. However, the values of accumulated equivalent plastic strain differ by more than one order of magnitude from 0.005 in the 90°-ply to 0.018 in the $-45°$-ply position. Both contour diagrams show a X-shaped strain distribution. This is an expected result for the $-45°$-ply as reported for example by Flatscher et al. [55] for a pure ±45°-layup. The plastic strain in the 90°-ply, which is located between the two 45°-plies, also seems to be dominated by the surrounding 45°-plies.

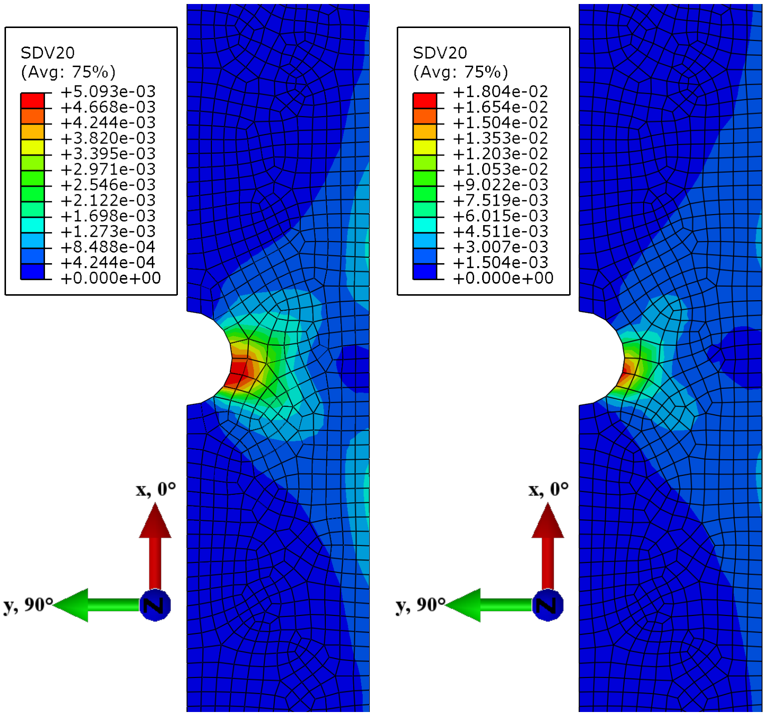

(a) $\tilde{p}$ in 90°-ply

(b) $\tilde{p}$ in -45°-ply

Figure 16: Accumulated plastic strain at point A in open-hole tension specimen with $d = 5$ mm

4.5.3. Detailed comparison of progressive damage analyses with Cuntze's FMC and Puck's APSC

The detailed comparison of the progressive damage analyses with Cuntze's FMC and Puck's APSC is performed at the example of the open-hole tension specimen with a hole diameter $d = 5$ mm and a width $w = 20$ mm. However, the findings hold true also for the other specimens analysed. In Fig. 17 the resulting load-displacement curves from both analyses are plotted. It can be observed that the predicted stiffness of the specimen is the same for both versions of the material model. As with all analysed specimens, the predicted failure load with the APSC is bigger than the load predicted by the FMC. In order to gain further insights, the damage initiation points are marked in the diagram. The initial transverse matrix damage is marked by an A and B marks the first matrix damage in shear. The start of fibre damage is marked with point C. The subscript $\square_P$ assigns the points belonging to the prediction with Puck's APSC and the subscript $\square_C$ to the one with Cuntze's FMC. It can be seen that the transverse matrix damage initiates at nearly the same load level. The in-plane shear matrix damage with the material model using Puck's APSC (B_P) starts at the same load level as transverse matrix damage (A_P) due to the formulation of damage variables. This point is predicted much later with Cuntze's separate formulation for interfibre failure under shear stress (IFF3), cf. B_C. Although the fibre failure criterion is the same for both theories, the predicted fibre damage initiation is slightly different. This may result from different interfibre damage progression and consequently varying load redistributions. The deviation in the predicted failure load may also be attributed to this behaviour.

In order to assess the influence of the additional iterative fracture angle search as well as the additional algorithms to divide the damage portions from the interfibre fracture according to the fracture angle between the different stress components the computational expenses of the simulations with the FMC and the APSC are compared. At this point it should be mentioned that the fracture angle search causes the majority of the additional computing time. All simulations were performed with the same solver settings on a workstation with two Intel Xeon E5-2643 processors (4 CPU cores, 10 MB Cache, 3.3 GHz per processor) and 32 GB RAM using two CPU cores. The models consist of about 15000 elements with about 55000 equations in total. The results regarding number of increments, the total CPU time and the average time per increment are listed

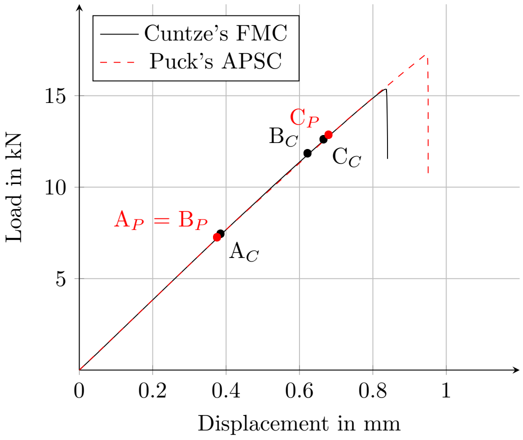

Figure 17: Comparison of predicted load-displacement curves of AS4/PEEK $[0/45/90/-45]_{2s}$ open-hole tension specimens ($d = 5$ mm, $w = 20$ mm)

in Tab. 8.

Table 8: Comparison of computational expense of proposed material model with different failure criteria on the basis of an open-hole tension specimens (QI, $w = 20$ mm)

Failure criterion	d in mm	Nr. of increments	Total CPU time in s	Average time per increment in s
Cuntze's FMC	2	1231	60349	49.02
	3	1212	36363	30.00
	5	1162	31690	27.27
	8	993	24641	24.81
	10	548	12786	23.33
Puck's APSC	2	1492	113233	75.89
	3	1601	96726	60.42
	5	6965	240945	34.27
	8	2128	67144	31.55
	10	24837	682476	27.48

It can be seen that the analysis of the same model model takes always more increments as well as more CPU time when using the APSC. The higher number of increments needed for the model with Puck's APSC can partly be attributed to the fact that the load bearing capacity is preserved for a longer time after the damage has been initiated compared to the prediction with Cuntze's FMC. This effect is intensified by the fact that the time step decreases with the onset of the damage. Furthermore, the average time per increment is always higher if the APSC is used. This can be explained by the additional effort required for the iterative fracture angle search and the split of the interfibre damage. The model with the FMC from Cuntze is, as expected, more efficient in the calculation. Measures to increase the numerical efficiency of the APSC, such as the golden section search [56, 57] are not considered in this work. They shorten the computing time but, unlike the FMC, still require additional algorithms.

5. Conclusions

A combined elastoplastic CDM-based damage model for solid elements has been proposed in this work. The main components of the model are a one parameter plasticity model from Sun and Chen [23] and Cuntze's FMC [28]. For comparison, also a version of the material model with Puck's APSC has been proposed and implemented. The analysis of a tensile test specimen made from AS4/PEEK with a $[\pm 45]_{2s}$-layup shows the necessity to account for plasticity in the progressive damage analysis of fibre composite materials with tough matrix materials. The validation with open-hole tension tests points out that the non-linear behaviour prior to first damage of the specimen is well reproduced by both version of the material model. In addition, the proposed material model allows an accurate prediction of the failure behaviour and strength of open-hole tension specimens with different geometries and d/w-ratios both with the FMC from Cuntze and with the APSC from Puck. It was highlighted that analyses with the FMC usually yield conservative strengths, while the failure load is overestimated by the APSC in most cases. The analysis results of one test specimen ($w = 20$ mm, $d = 5$ mm) were compared in more detail. The results show that the prediction of the first transverse matrix damage and the first fibre failure is almost identical with both failure theories. However, the prediction of matrix damage under shear stress is different. With the FMC, the degradation of the shear modulus begins at a significantly higher load. Using this example it can also be demonstrated that the FMC is numerically more efficient than the APSC since the time-consuming iterative fracture angle search is no longer necessary.

Validation with own experimental results and a different material, preferably with failure criterion parameters determined for this material, would be beneficial. In this context, further data for example from digital image correlation and acoustic emission measurements, could also be used for even more in-depth validation.

Acknowledgements

This project has received funding from the European Union's Horizon 2020 research and innovation programme under the Grant Agreement No. 807097.

References